



HIDING IN THE SHADOWS. II. COLLISIONAL DUST AS EXOPLANET MARKERS

JACK DOBINSON^{1,2}, ZOË M. LEINHARDT¹, STEFAN LINES¹, PHILIP J. CARTER¹,

SARAH E. DODSON-ROBINSON³, AND NICK A. TEANBY²

¹ University of Bristol, School of Physics, H. H. Wills Physics Laboratory, University of Bristol, Bristol BS8 1TL, UK

² University of Bristol, School of Earth Sciences, H. H. Wills Physics Laboratory, University of Bristol, Bristol BS8 1TL, UK

³ University of Delaware, Department of Physics and Astronomy, 217 Sharp Lab, Newark, DE 19716, USA

Received 2015 June 29; accepted 2016 January 7; published 2016 March 15

ABSTRACT

Observations of the youngest planets ($\sim 1\text{--}10$ Myr for a transitional disk) will increase the accuracy of our planet formation models. Unfortunately, observations of such planets are challenging and time-consuming to undertake, even in ideal circumstances. Therefore, we propose the determination of a set of markers that can preselect promising exoplanet-hosting candidate disks. To this end, N -body simulations were conducted to investigate the effect of an embedded Jupiter-mass planet on the dynamics of the surrounding planetesimal disk and the resulting creation of second-generation collisional dust. We use a new collision model that allows fragmentation and erosion of planetesimals, and dust-sized fragments are simulated in a post-process step including non-gravitational forces due to stellar radiation and a gaseous protoplanetary disk. Synthetic images from our numerical simulations show a bright double ring at $850\ \mu\text{m}$ for a low-eccentricity planet, whereas a high-eccentricity planet would produce a characteristic inner ring with asymmetries in the disk. In the presence of first-generation primordial dust these markers would be difficult to detect far from the orbit of the embedded planet, but would be detectable inside a gap of planetary origin in a transitional disk.

Key words: methods: numerical – planet–disk interactions – protoplanetary disks

1. INTRODUCTION

Over the last 20 years more than 1900 exoplanets have been discovered with a huge diversity in system parameters. These discoveries imply that planet formation is a ubiquitous phenomenon. In order to discriminate between different models of planet formation, observations of evolved planetary systems are of great utility. However, due to the chaotic nature of planetary dynamics, many formation models produce end results that are indistinguishable. Observations of young exoplanets would discriminate between formation models, as suggested by Setiawan et al. (2007) and Hernán-Obispo et al. (2010).

Unfortunately, observations of young planets are challenging because of their environment. Radial velocity methods lose sensitivity due to the inherent variability of the host star (Saar & Donahue 1997) and transit detection and direct imaging methods can be rendered impossible as the planet is obscured by a cloud of dust and gas. One solution to the observational difficulties posed by young star–disk systems is to search for indirect planet indicators based on interaction with disk dust and gas.

Determining the physical significance of dust structures in transitional and pre-transitional disks is not a new idea. One of the oldest examples of a predicted dust structure is a gap in a protoplanetary disk caused by the direct gravitational influence of a planet (Goldreich & Tremaine 1980). The morphology of a gap can be used to infer properties of the disk (Paardekooper & Mellema 2004; Crida et al. 2006; Fouchet et al. 2007), with large gaps being indicative of either massive companions or multiple companions (Dodson-Robinson & Salyk 2011; Espaillet et al. 2014, p. 497; Dong et al. 2015). In early studies, because of numerical constraints, it was assumed that the dust and gas in a disk were well mixed, and models of observations still use this method (D’Alessio et al. 1998; Ruge et al. 2014). However, due to the imperfect coupling of larger dust grains to

the gas, it is argued that the observed structures vary with wavelength (Rice et al. 2006; Gonzalez et al. 2012; Pinilla et al. 2012; Zhu et al. 2012). To investigate the effect of imperfect dust–gas coupling, two fluid models coupled with radiative transfer modeling are employed (Fouchet et al. 2010; Zhu et al. 2012; Owen 2014; Pinilla et al. 2014, 2015). One important result from two fluid models is the trapping of dust in a planet-induced pressure bump. A pressure bump will reduce the mass of large dust grains interior to the bump; therefore the millimeter-wavelength signal is reduced such that a cavity is observed. Deeper gaps and cavities are observed when dust trapping operates in concert with an additional clearing mechanism (Paardekooper & Mellema 2006; Fouchet et al. 2007; Zhu et al. 2012).

The mutual interaction between planets, dust, and gas has also been investigated by the N -body community. The mid to late stages of planet formation are not fully captured by hydrodynamical or N -body approaches alone. As such, combined N -body and Hydro codes are now being used to investigate this epoch as the computational power has only recently become available (Lambrechts & Johansen 2012; Levison et al. 2012, 2015). One notable result from the coupling of N -body and Hydro codes is the model of pebble accretion. Pebble accretion relies upon the imperfect (non-negligible, but not dominating) coupling of centimeter-sized particles with gas to efficiently accrete mass onto seed planetesimals (Johansen & Lacerda 2010; Ormel & Klahr 2010; Lambrechts & Johansen 2012). The generation of dust from interactions between planetesimals has been investigated in relation to debris disks (see Wyatt 2008; Thebault et al. 2014), the modeling of giant impacts (e.g., Kral et al. 2013), and the simulation of the mid to late stages of planet formation (e.g., Leinhardt & Stewart 2012; Leinhardt et al. 2015). The methods used range from almost purely statistical (Wetherill & Stewart 1989; Morbidelli et al. 2009; Bromley & Kenyon 2011)

to purely N -body (Chambers & Wetherill 1998; Kokubo & Ida 2000; Raymond et al. 2009), with many groups employing a mixture of the two (Spaute et al. 1991; Weidenschilling et al. 1997; Bromley & Kenyon 2011).

Our first paper, a proof of concept (Dobinson et al. 2013, hereafter Paper 1), showed that a planetary companion can influence the dust distribution of a planetesimal disk. Numerical simulations of gas-free planetesimal disks with an embedded planet of varying eccentricity were conducted with the N -body code PKDGRAV (Richardson et al. 2000; Stadel 2001; Leinhardt et al. 2009). The simulations included a planetesimal collision model, RUBBLE, that enabled tracking of growth and disruption of planetesimals and large collision fragments. Collisionally generated second-generation dust from planetesimal collisions was modeled in a simple post-processing step. Dust was assumed to sit on an “average” orbit determined from the orbits of both its parent bodies, and did not evolve (i.e., the orbital parameters and grain sizes could not change after creation). By comparison with an undisturbed control disk, the presence of a planet was shown to have the capability to enhance the visibility of the system and create asymmetries in the dust disk.

The work presented here addresses the main deficiencies of Paper 1 (assumed average orbits and no evolution of dust) by significantly increasing the realism of the numerical scenarios and producing more accurate and useful constraints. The main simulations contain an updated, faster analytical collision model called EDACM (Leinhardt & Stewart 2012; Leinhardt et al. 2015), and second-generation dust is simulated in a more physical manner where both distribution of ejection velocity and lifetime are accounted for. In order to increase the realism, non-gravitational forces acting on the second-generation dust are also included, such as gas drag from complementary hydrodynamical simulations using the FARGO code (Masset 2000), photon pressure, and Poynting–Robertson drag. These upgrades provide a more accurate description of the collisional environment present near a planet in a transitional disk. See Section 2 for a more complete discussion. The results of these simulations are presented in Section 3. First-generation primordial dust is excluded from the simulations, but its effect upon observability of the second-generation dust is discussed in Section 4. We give our conclusions in Section 5.

2. NUMERICAL METHODS

The numerical techniques used in this investigation can be split into four discrete sections, briefly summarized below and discussed in detail in the subsections identified.

1. Planetesimal disk (Section 2.1). N -body simulations including particle–particle collisions, a perturbing planet, and interparticle gravity are used to model the planetesimal population (particles ≥ 100 km).
2. Gas disk (Section 2.2). Hydrodynamical simulations including an embedded planet are used to provide maps of gas density and velocity for fragment simulations. This is needed as collisions in the planetesimal disk produce fragments small enough to be affected by aerodynamic drag.
3. Dust (Section 2.3). Small-sized (10^{-2} – 10^{-5} m) collisional debris from the planetesimal disk simulations is integrated directly with additional external forces due to gas and radiation. These fragments would be very small

Table 1
Properties of the Planetesimal Simulation

Name	Collision Model	M_{pl}	T_{grow} (yr)	e_{pl}	T_{final} (yr)	$N_{\text{Collisions}}$
Prelim	Merging ^a	3.29×10^4	...
Control	EDACM	2×10^4	9688
Ecc0	EDACM	$1M_J$	100	0.0	2×10^4	13511
Ecc1	EDACM	$1M_J$	100	0.1	2×10^4	9498
Ecc2	EDACM	$1M_J$	100	0.2	2×10^4	11156

Note.

^a This simulation formed the starting point for the others.

in reality with no significant self-gravity, thus they are modeled as test particles that feel the gravitational influence from the star and planet only. Planetesimals are not included.

4. Synthetic observations (Section 2.4). Dust lifetime, image construction, and radiative transfer modeling are used to create synthetic images and identify observables such as NIR excess, disk asymmetries, and gaps that would indicate the presence of an unseen planet.

The planetesimal and gas disk are treated as separable and numerically modeled independently, but the results of both are required in order to model the dust and create the synthetic images.⁴

2.1. Planetesimal Disk Simulations

The evolution of the planetesimal disk is numerically modeled using a modified version of the parallelized hierarchical tree code PKDGRAV. This code uses a second-order leapfrog integrator, which is symplectic in the absence of the gravity tree. The equations of motion for the particles are determined by gravity and physical collisions.

Each simulation begins with 10^6 equal-mass planetesimals of 150 km radius with a bulk density of 2 g cm^{-3} in a circumstellar disk extending from 0.8 to 10 AU around a $1 M_{\odot}$ central potential. The planetesimals were initially distributed assuming a minimum-mass solar nebula (Weidenschilling 1977; Hayashi 1981; Hayashi et al. 1985) such that the surface density has a standard power-law distribution, $\Sigma(r) = \Sigma_1 r^{-1.5}$, where $\Sigma_1 = 10 \text{ g cm}^{-2}$ at 1 AU, resulting in a total planetesimal mass of $10M_{\oplus}$. Eccentricities and inclinations were drawn from a Rayleigh distribution with dispersion $\langle e^2 \rangle = 2 \langle i^2 \rangle = 0.001$ (Richardson et al. 2000).

In order to create a more realistic and evolved planetesimal size distribution than the initial uniform distribution, the initial planetesimal disk was integrated using a collision model with perfect merging (no fragmentation or erosion) and no embedded planet. This preliminary simulation was integrated until the particle number had reduced by two thirds to $N = 3 \times 10^5$ (Table 1, row 1). The power-law distribution of surface density, $\Sigma(r) \propto r^{-1.5}$, is retained, and the size distribution is no longer single-valued (as it was in Paper 1) but is an approximate power law of the form $n(r)dr \propto r^{-3.5}$, with planetesimal radii ranging from the initial 150 km to ~ 1000 km.

⁴ All numerically intensive work was carried out using the computational facilities of the Advanced Computing Research Centre, University of Bristol (<http://www.bris.ac.uk/acrc>).

After the preliminary phase of perfect merging a planet core is embedded in the planetesimal disk and the collision model is switched to EDACM, which allows multiple collision outcomes. EDACM consists of a set of scaling laws and collision outcome rules based on data from a series of direct numerical simulations of individual collisions (both N -body and hydrodynamical) that characterize the collision type, largest remnants, and fragment size distribution (see Leinhardt & Stewart 2012). EDACM can identify and resolve several collision types including erosion (partial and supercatastrophic), accretion (perfect and partial), and hit-and-run (perfect/bouncing and disruption of the projectile). To reduce computational complexity, these simulations incorporated a size limit. Only fragments larger than 30 km in radius were directly simulated; smaller debris was recorded in 10 axisymmetric annular “dust bins” extending from 0.3 to 10.5 AU (Leinhardt & Richardson 2005; Leinhardt et al. 2015).

In order to incorporate EDACM into PKDGRAV and make the collision model as effective as possible for the tasks presented in this work, modifications were made to EDACM to describe the positions and velocities of the collision fragments as accurately as possible (see Leinhardt et al. 2015 for details). For self-consistency the modifications to EDACM were derived from the same underlying data used in the development of EDACM.

In this work we completed four main N -body planetesimal disk simulations—three with an embedded Jupiter-mass planet and one without to serve as a control case. Given the broad range of exoplanet eccentricities, the eccentricity of the embedded planet was varied (see Table 1).

All disks had the same starting point—the end of the Prelim simulation. The embedded planet (when present) was placed at a semimajor axis of 2.8 AU such that the simulation could capture all perturbations from the planet, because eccentricity boosting of the planetesimals can be seen far from the planet’s orbit. Only one planet is present in the system. Therefore, it is simple to scale the results to any system geometry.

In order to avoid numerical errors from large impulses upon planetesimals near the planet, the embedded planet is grown within the planetesimal disk from $15 M_{\oplus}$ to $1 M_J$ over 100 yr. Note that the timescale of growth is not physical—it is a factor of 1000 faster and is used here primarily to create as realistic an initial condition as possible in a practical amount of time (for more details see Paper 1).

All planetesimal simulations ignore the gas disk. The mass of gas is only a small fraction of the stellar mass, and any gravity from it can be ignored to the first order (Hartmann et al. 1998). In addition, the planetesimals are all initially >150 km in radius, thus drag forces upon them are insignificant over the simulation timescale due to their size.

Each of the planetesimal simulations was run for 2×10^4 yr; the timescale could not be too long due to numerical constraints but was made long enough to provide two dust half-lives (see Section 2.3). The time step was set to 0.01 yr, which provided good temporal resolution in all areas of the planetesimal disk.

2.2. Gas Disk Simulations

Planetesimals are not influenced dynamically by the gaseous component of a circumstellar disk. However, small fragments produced in a collision are. Therefore, hydrodynamical simulations of the gaseous component were performed using the FARGO code for each of the system configurations under

investigation. FARGO is a 2D Eulerian polar grid code that is widely used to model astrophysical disks. These simulations used an initial surface density of $\Sigma(r) = \Sigma_{1g} r^{-0.5}$, with $\Sigma_{1g} = 1780 \text{ g cm}^{-2}$, an aspect ratio of 0.05, and an α -viscosity of 2×10^{-3} , similar to the values used by Zhu et al. (2012). To avoid edge effects the FARGO simulations extend beyond the dimensions of the planetesimal disk from 0.4 to 50 AU. A $1 M_J$ planet is positioned at 2.8 AU (coincident with the planetesimal disk simulations). The system is integrated for 1×10^4 yr until it reaches a steady state.

Note that the planetesimal disk is assigned a different surface density profile than the gas disk. This is because, as we are assuming that the core-accretion model is correct, the growth timescale of the planetesimals scales with semimajor axis, resulting in faster growth in the inner regions of the disk when compared to the outer regions (Paardekooper & Leinhardt 2010). Thus, the surface density profile of the ~ 100 km planetesimals should be more centrally peaked than the gas profile. To reflect this, we have used the minimum-mass solar nebular model for the planetesimal surface density, giving $\Sigma(r) \propto r^{-1.5}$ (Hayashi 1981), and have assumed a constant aspect ratio (Takami et al. 2014) and accretion rate for the gas disk, which leads to the $\Sigma(r) = \Sigma_{1g} r^{-0.5}$ surface density profile (Zhu et al. 2012).

2.3. Dust Model

The planetesimal disk simulations can cope with erosion and fragmentation of a planetesimal. However, by necessity a size limit was imposed upon the simulated particles. Therefore, small collision fragments were simulated in a secondary code, the fragment simulation engine (FSE). The FSE takes the collisions from a planetesimal disk simulation, models the trajectories of the small fragments using a modified version of the EDACM model (Leinhardt et al. 2015), and simulates their orbits.

A second-order leapfrog integrator is used, similar to the one used in PKDGRAV with a time step of 0.01 yr. Technically, any size of fragment can be simulated, but in this work we restrict ourselves to small fragments, as interfragment gravity is not included. Fragments of sizes 10^{-3} – 10^{-5} m are simulated because it is millimeter- to micron-sized particles that have the largest effect upon visibility in the radio and infrared, wavelengths in which transitional disks are typically observed (see Section 2.4 for more details).

Small particles simulated by FSE are affected by gas drag. Therefore, the gas disk simulations (Section 2.2) provide the gas properties at all positions in the simulated protoplanetary disk. In the planetesimal disk simulations the planetesimals are large enough that to first order the direct effects of gas can be ignored but interparticle gravity cannot. When modeling the dust the opposite is true, namely, the dust particles are small so aerodynamic drag from the gaseous accretion disk will affect the orbits of the smallest collision fragments. This is incorporated into the force calculations by the drag equation

$$\mathbf{F}_d = \frac{-\rho_g (\Delta \mathbf{v})^2 A C_d}{2}, \quad (1)$$

where \mathbf{F}_d is the drag force, $\Delta \mathbf{v}$ is the difference in fragment and gas velocities, ρ_g is the gas density, A is the cross-sectional area of a fragment in the direction of travel (we assume a sphere), and C_d is the drag coefficient, which varies depending upon the

drag regime (Weidenschilling 1977), i.e.,

$$C_d = \frac{8}{3} \frac{\bar{v}}{v} \quad \text{in the Epstein regime,}$$

$$C_d = 24Re^{-1} \quad \text{for } Re < 1,$$

$$C_d = 24Re^{-0.6} \quad \text{for } 1 < Re < 800,$$

$$C_d = 0.47 \quad \text{Otherwise.}$$

Here \bar{v} is the thermal velocity of the gas, Re denotes the Reynolds number of the flow, and the Epstein regime is characterized by the dust radius, $a < (9/4)\lambda$, where λ is the mean free path of a molecule.

Due to the size range of material simulated it is necessary to include photon pressure and Poynting–Robertson drag in addition to the aerodynamic drag from the gas disk. The photon pressure is included as an additional force following Nichols & Hull (1903):

$$\mathbf{F}_{\text{phot}} = \beta F_G (1 - \mathbf{v} \cdot \hat{\mathbf{r}}) \hat{\mathbf{r}}, \quad (2)$$

where

$$\beta = \frac{3L_*}{16\pi G M_* c a \rho} \quad (3)$$

is the ratio between radiation forces and gravitational forces for a given particle, L_* is the stellar luminosity, G the gravitational constant, M_* the stellar mass, a the radius of the particle, ρ the density of a particle, c the speed of light, F_G the gravitational force of the star, \mathbf{v} the velocity of a particle, and $\hat{\mathbf{r}}$ the unit radial vector from star to particle.

Poynting–Robertson drag (Robertson 1937; Burns et al. 1979) is included in FSE as

$$\mathbf{F}_{\text{PR}} = \beta F_G (-\mathbf{v}), \quad (4)$$

where the symbols have the same definition as above.

In FSE, fragments are modeled as test particles and do not feel gravity from other test particles. The central star and embedded planet are modeled as gravitating particles (gravity-producing and gravity-feeling); collision detection is not included in the simulation. As test particles have no mutual interaction, FSE lends itself to massive parallelization, and each run was split across 100 cores with each core simulating a different set of collisions that were detected in the main planetesimal simulations (Section 2.1). Every collision was assigned 100 test particles to follow the velocity field of the fragments found by the modified EDACM model. Each set of collisions was simulated three times (Table 2): no gas with small particles (10 μm), gas with small particles, and gas with large particles (1 cm).

2.4. Synthetic Observations

The Fragment Image Reconstruction Engine (FIRE) creates images from FSE, PKDGRAV, and FARGO output files, and also creates RADMC3D input files. FSE files provide the dust density information for maps and RADMC3D input, FARGO files provide gas density maps, and PKDGRAV files ensure alignment between different maps. Dust lifetime algorithms are applied to collision fragments.

The visibility of dust is directly related to its size. FSE simulates dust grains in a specific size range, and any material outside that size range is assumed to be non-visible. The size of dust can be changed by two main pathways: fragmentation to a

Table 2
Properties of the FSE Simulation

#	Parent ^a	Gas	Frag. Size (m)	$N_{\text{collisions}}$ ^b	Figure
1	Control	No	1×10^{-5}	9688	...
2	Control	Yes	1×10^{-5}	9688	Figure 6
3	Control	Yes	1×10^{-3}	9688	...
4	Ecc0	No	1×10^{-5}	13511	...
5	Ecc0	Yes	1×10^{-3}	13511	Figure 2
6	Ecc0	Yes	1×10^{-3}	13511	...
7	Ecc1	No	1×10^{-5}	9498	...
8	Ecc1	Yes	1×10^{-5}	9498	Figure 7
9	Ecc1	Yes	1×10^{-3}	9498	...
10	Ecc2	No	1×10^{-5}	11156	...
11	Ecc2	Yes	1×10^{-5}	11156	Figure 3
12	Ecc2	Yes	1×10^{-3}	11156	...

Notes.

^a The planetesimal simulation from which we use the collisions.

^b The number of collisions in the parent simulation.

smaller size or coagulation to a larger size. Note that physical removal of dust via Poynting–Robertson drag, photon pressure, and gas drag is accounted for in the FSE. The exact balance between fragmentation and coagulation of dust is unknown and is an ongoing area of research but makes a large difference in the “visibility lifetime” of the dust. If dust never changes size then growth to protoplanets would be impossible, whereas if dust rapidly changes size the observable signatures of protoplanetary disks would quickly dissipate. To model the change in dust size via fragmentation and coagulation we assume that the “visibility lifetime” can be treated as an exponential decay.

The “visible” mass, dependent upon a decay constant, is varied as

$$P_{\text{vis}}(t) = e^{(T_{\text{creation}} - t)/\lambda}, \quad (5)$$

where $P_{\text{vis}}(t)$ is the fraction of visible dust mass at simulation time t , T_{creation} is the creation time of the particle, $t > T_{\text{creation}}$, and λ is the e -folding timescale. This represents a certain proportion of available grains becoming non-visible in some way (Dullemond & Dominik 2005). In this work $\lambda = 10^4/\ln(2)$ yr, resulting in a half-life of 10^4 yr (Adams et al. 2004).

The mass of dust from each collision was found by assuming a power-law distribution of $n(r)dr = \eta r^{-3.5}dr$ (where η is a normalising factor), which gives the mass of dust between the sizes $r_1 = 1 \times 10^{-3}$ m and $r_2 = 1 \times 10^{-5}$ m as

$$M(r_1, r_2) = \eta' (r_1^{0.5} - r_2^{0.5}), \quad (6)$$

where $r_1 > r_2$, and η' is a different normalizing factor found via $\eta' = M_{\text{rem}} M_{\text{slr}}^{-0.5}$, where M_{slr} is the mass of the second largest remnant computed via the EDACM code, and $M_{\text{rem}} = M_{\text{total}} - (M_{\text{lr}} + M_{\text{slr}})$ is the mass that would become debris (i.e., mass not included in the largest and second largest remnants of a collision). Therefore, net erosive collisions will contribute more to the mass of dust in a system than net growth collisions. The mass found via Equation (6) scales the mass of the tracer particles.

From the dust density, synthetic images were obtained using the radiative transfer code RADMC3D. Small dust was modeled as two dust species, amorphous carbon and silicates,

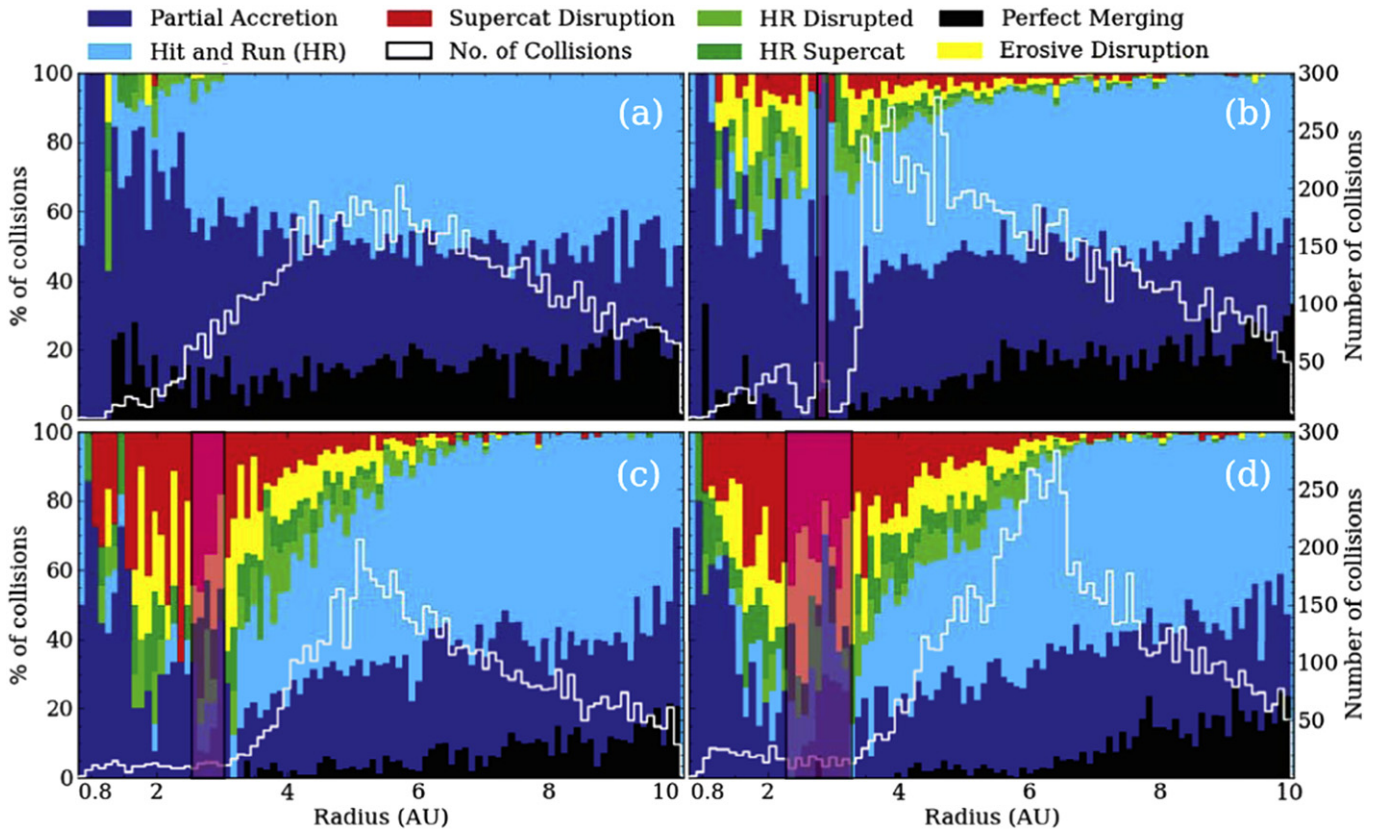


Figure 1. Fraction of collision type with radius for the Control simulation (a), and main simulations Ecc0 (b), Ecc1 (c), Ecc2 (d). Collision type is indicated by the color key above (a) and (b); the height of the stacked bars indicates what fraction of the total number of collisions is of which type (left-hand axis). The white line shows the number of collisions in each bin (right-hand axis). The planet is situated at 2.8 AU, and has an eccentricity of 0.0, 0.1, and 0.2 in frames (b), (c), and (d) respectively, the orbital range of the planet is depicted with the magenta area.

at $0.1 \mu\text{m}$ and $0.631 \mu\text{m}$; the species have relative abundances of 0.2 and 0.8 respectively, in line with interstellar dust (Kruegel 2003, Section 12.4.1). Larger dust from 1 to $1000 \mu\text{m}$ is modeled using simple Mie scattering spheres with three size bins per decade.

Dust of all sizes should be created in a collision. However, the smallest size is approximately defined by the dust blow-out radius, and the largest is when emission at IR wavelengths (used for observing exozodis) and submillimeter wavelengths (in which transitional disks are typically observed) is no longer significant.

3. RESULTS

Figure 1 shows the collision type versus disk radius at the end state of the four main simulations. Collisions were summed over time and binned as a function of semimajor axis for the Control, Ecc0, Ecc1, and Ecc2 simulations (Table 1), each of which provides collision data for three FSE simulations (Table 2). Colors denote the type of collision, with proportions shown by stacked bars relating to the left-hand y-axis; the white line shows the number of collisions in a given bin relating to the right-hand y-axis. Collision types are as follows: perfect merging—colliders merge inelastically and no debris is produced, partial accretion—debris is produced but there is net growth of one collider, erosive disruption—debris is produced and one or both colliders are smaller, supercatastrophic disruption—debris is produced and neither collider survives, hit-and-run—colliders bounce without changing

mass, hit-and-run disrupted—the smaller collider is eroded and produces dust while the larger collider is unaffected, hit-and-run supercatastrophically disrupted—the smaller collider is destroyed and produces dust while the larger collider is unaffected. The collisions shown in Figure 1 are only planetesimal–planetesimal collisions and do not include collisions with the $1M_J$ planet; collisions with the planet are purely accretive and do not produce any debris.

The total number of collisions (white line, right-hand scale) is approximately equal for each simulation (see Table 2). However, the radial distribution is very different. For simulations including a planet (b)–(d) the region near the planet at 2.8 AU has fewer collisions than the control case (a). The peak in the number of collisions is comparable or larger in number. The reduction near the planet coincides with an increase in destructive collisions, and the peak is shifted to a larger radius where there are fewer destructive collisions. We suggest that the reduction in collision number is due to stirring from a planet causing highly destructive collisions in its vicinity, such that planetesimals experience few collisions before destruction. The shifting of peak collisions is also due to stirring from the planet, but of a lower magnitude. Planetesimals are disturbed so that they collide with increased frequency but with low enough velocities that they survive the encounters.

Erosive collisions (greens, yellow, and red) become more frequent throughout the radial extent of the disk when the planetary perturber is introduced, and increase in frequency with eccentricity. Also, the proportion of non-erosive collisions (blues and blacks) decreases in the same manner, or remains

steady. The increase in erosive collisions due to the presence of a planet is attributed to the higher level of gravitational stirring, which pumps up the mutual velocities of the planetesimals, increasing the number of energetic collisions; this also explains the decrease in non-erosive collisions, as these are generally of lower energy. The extra erosive collisions caused by a more eccentric planet are due to the same mechanism, but in a more extreme way. The planet can influence more planetesimals and put them onto more eccentric orbits, which increases the collision energies more so than a non-eccentric planet.

Figures 2 and 3 show the main results from simulations 5 and 11. From the top the rows are: planetesimal position from PKDGRAV simulations, gas surface density from FARGO simulations, dust surface density from the FSE secondary simulations, $10\ \mu\text{m}$ flux, and $850\ \mu\text{m}$ flux computed with the RADMC3D radiative transfer code. The columns increase in time from left to right. Similar figures for simulations 2 and 8 can be found in Figures 6 and 7.

In Figures 2 and 3 the planetesimal position and gas density show the clearing of a gap coincident with the planet’s orbit. As expected, the gap is larger but shallower in the eccentric case. At later times the gap becomes cleaner due to particle growth and collisional destruction, which removes material; this is more noticeable in the eccentric case.

However, the frames for dust surface density do not show as much clearing as those for the planetesimal position and gas density. The non-eccentric case (sim. 5, Figure 2) has a narrow ring of cleared space, whereas the eccentric case (sim. 11, Figure 3) has two brighter inner and outer rings with a lower surface density between them. In both cases there are two brightness peaks, one interior and one exterior to the planet’s orbit. This is similar to the structures found in Paper 1. However, disk asymmetry is less pronounced in this work because these simulations account for the eccentricity distribution of the second-generation dust rather than assuming a single orbit.

The flux density frames, both 10 and $850\ \mu\text{m}$, show an increase in peak flux between the non-eccentric (sim. 5) and eccentric (sim. 11) cases. This is due to the previously mentioned dust rings interior and exterior to the planetary orbit. In the eccentric case (sim. 11) the inner ring is closer to the star and therefore hotter, thus contributing more to the flux. Additionally, the eccentric planet forces planetesimals onto eccentric orbits, creating more dust (via more erosive collisions) and putting fragments on eccentric orbits, which increases the dust mass close to the star.

Figure 4 shows a spectral energy distribution (SED) of the emission from the disk compared to the emission from the star. The red “+” signs show the stellar emission, blue squares show Control simulation data, green dots show Ecc0 data, upright blue triangles show Ecc1 data, inverted purple triangles show Ecc2 data, and red lines (solid, dotted, dashed, and dotted-dashed) show decreasing fractions of the stellar flux.

Emission enhancement due to second-generation dust caused by the presence of the planet is easily seen. The peak emission from the no-planet case (sim. 2) is approximately 1/10 of the planetary emission (sims 5, 8, 11). The SEDs for the planetary simulations (dots and triangles) are so similar as to be practically indistinguishable even between the gaseous and non-gaseous cases. However, some trends between the planetary cases can be observed. As eccentricity increases, flux increases for the left and right frames. The central frame

has less distinction between eccentricities due to the small particle sizes being entrained in the gas disk. Observationally, the enhanced flux due to second-generation dust would be noticeable using nulling interferometry if collisional material was the only dust source present, but the Control case would not (see Section 4).

4. DISCUSSION

So far we have considered the case where second-generation dust is the only source of dust present in a transitional disk. This may not be the case if such disks retain some of their first-generation primordial dust, albeit at a lower surface density than their protoplanetary counterparts.

Figure 5 shows the surface density of simulated second-generation dust against the implied first-generation material present in the gas simulations. The solid red line shows the gas density, the dotted red line shows surface density of solid material assuming the usual 100:1 gas:solids ratio, the green shaded area shows an estimate for small ($<1\ \text{mm}$) first-generation dust, and blue bars show the second-generation dust from the simulations.

The estimate for small first-generation dust grains used the same power-law assumption as the size of collisionally generated material summarized in Equation (6) such that

$$M_{<1\ \text{mm}} = M_{\text{solid}}(r_1^{0.5} - r_2^{0.5})/(r_{\text{cut}}^{0.5} - r_2^{0.5}), \quad (7)$$

where M_{solid} is the mass of solid material assuming a 100:1 gas:solid mass ratio, $r_1 = 1 \times 10^{-3}\ \text{m}$ is the radius of the largest observable first-generation dust, $r_2 = 1 \times 10^{-5}\ \text{m}$ is the smallest first-generation dust, and $r_{\text{cut}} = 1 \times 10^5\ \text{m}$ is the cutoff below which we do not continuously simulate objects—in this case, our starting planetesimal size.

The upper limit of the green region, which shows an estimate of the mass of small ($<1\ \text{mm}$) first-generation dust, is found by applying Equation (7) to the estimate of solid material (red dotted line). The lower limit is found by assuming a lowering of gas surface density over the lifetime of a disk by an order of magnitude (Jones et al. 2012).

Second-generation dust from the no-planet case (sim. 2) would be rendered invisible by the large mass of first-generation material (and any first-generation material would be undisturbed). However, assuming a conservative estimate for the primordial material, the planetary cases (sims 5, 8, 11) see a comparable mass of first-generation to second-generation dust throughout the disk, and within the gaps second-generation dust is the dominant source. The zero-eccentricity case (sim. 5) would be the most obvious, with bright rings either side of the planet and a possible enhancement coincident with it. For more eccentric planets other markers such as asymmetries and dust structures would need to be relied upon.

The mass of first-generation dust estimated from Equation (7) assumes that the size distribution of growing dust and pebbles follows the same power law as planetesimals, and that dust coagulation leads to the formation of planetesimals. The well known centimeter and meter barriers (Weidenschilling 1977; Morbidelli et al. 2008) along with the fragility of $1\ \text{km}$ planetesimals (Leinhardt et al. 2009; Nelson & Gressel 2010) will perturb this power law, especially in the case of the centimeter barrier, which can result in mass “piling up” in smaller sizes. Also, if planetesimals are not constructed via dust coagulation, then pathways for the formation of gravitational

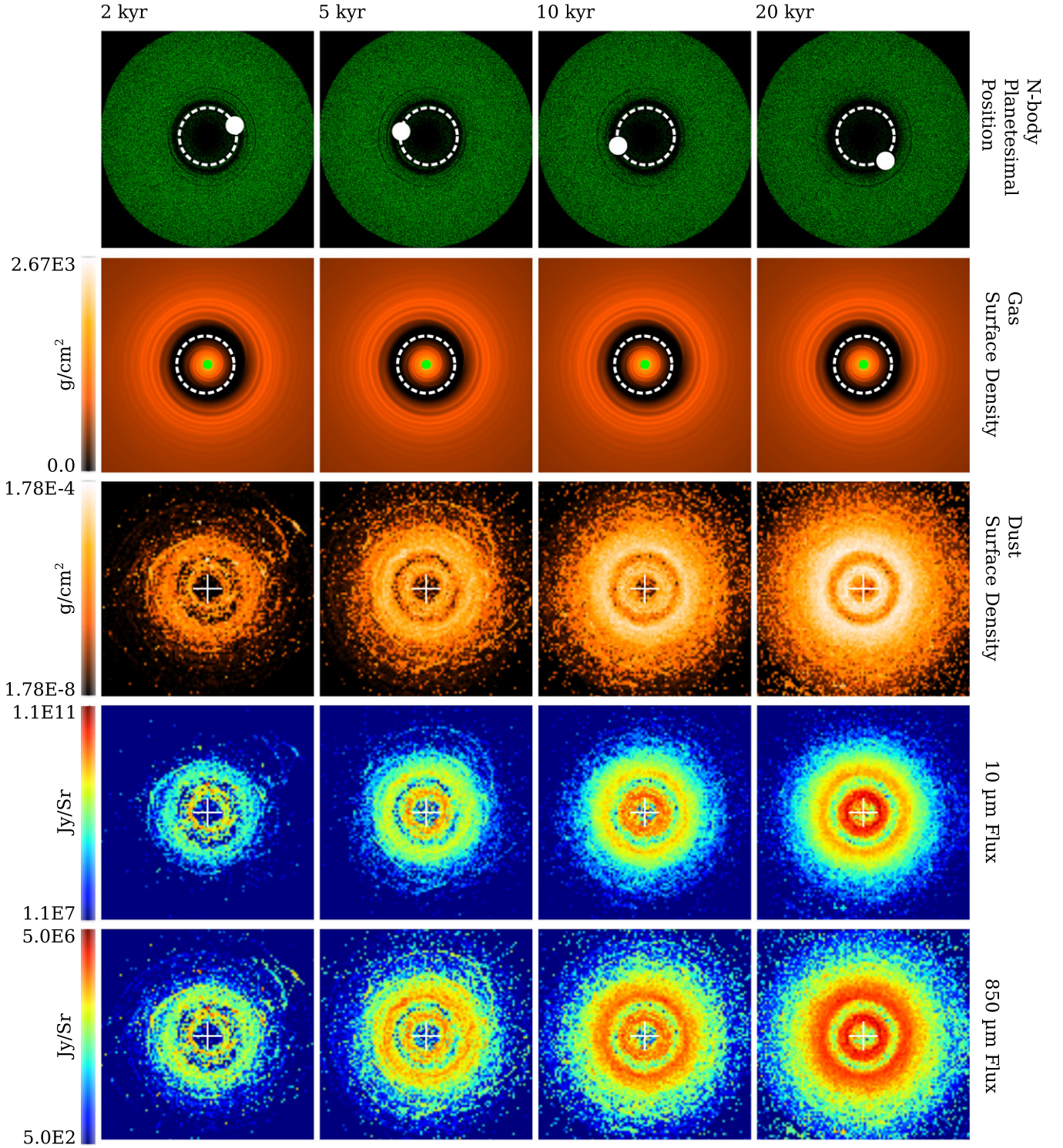


Figure 2. Summary of output from simulation 5. From top to bottom: positions of planetesimals over time, gas surface density from supporting FARGO simulations (green areas are outside the grid), dust surface density when lifetime is modeled as an exponential decay (decay constant of 10^4 yr), flux from dust (no stellar flux included) from radiative transfer modeling using RADMC3D at $10\ \mu\text{m}$ and at $850\ \mu\text{m}$. The white dotted line indicates the approximate orbit of the planet, the white circle indicates its approximate position, and the white cross indicates the barycenter of the system.

instability, such as turbulent concentration and streaming instability (e.g., Johansen et al. 2006; Cuzzi et al. 2008; Bai & Stone 2010; Gressel et al. 2011), can circumvent the growth of intermediate-sized objects completely such that Equation (7) no longer holds, even as an approximation.

Dust production (and therefore mass) is enhanced by the presence of a planetary body by a factor of ~ 10 (Figure 5).

Taken in combination with Figure 1, we conclude that in the no-planet case “Partial Accretion” (dark blue) collisions provide the main source of dust, whereas in the planetary case “Supercatastrophic” (red and dark green) collisions provide the main source and are much more efficient at dust production, as would be expected. For our scenario, the disk emission (Figure 4) is 1/100 of the stellar emission at peak

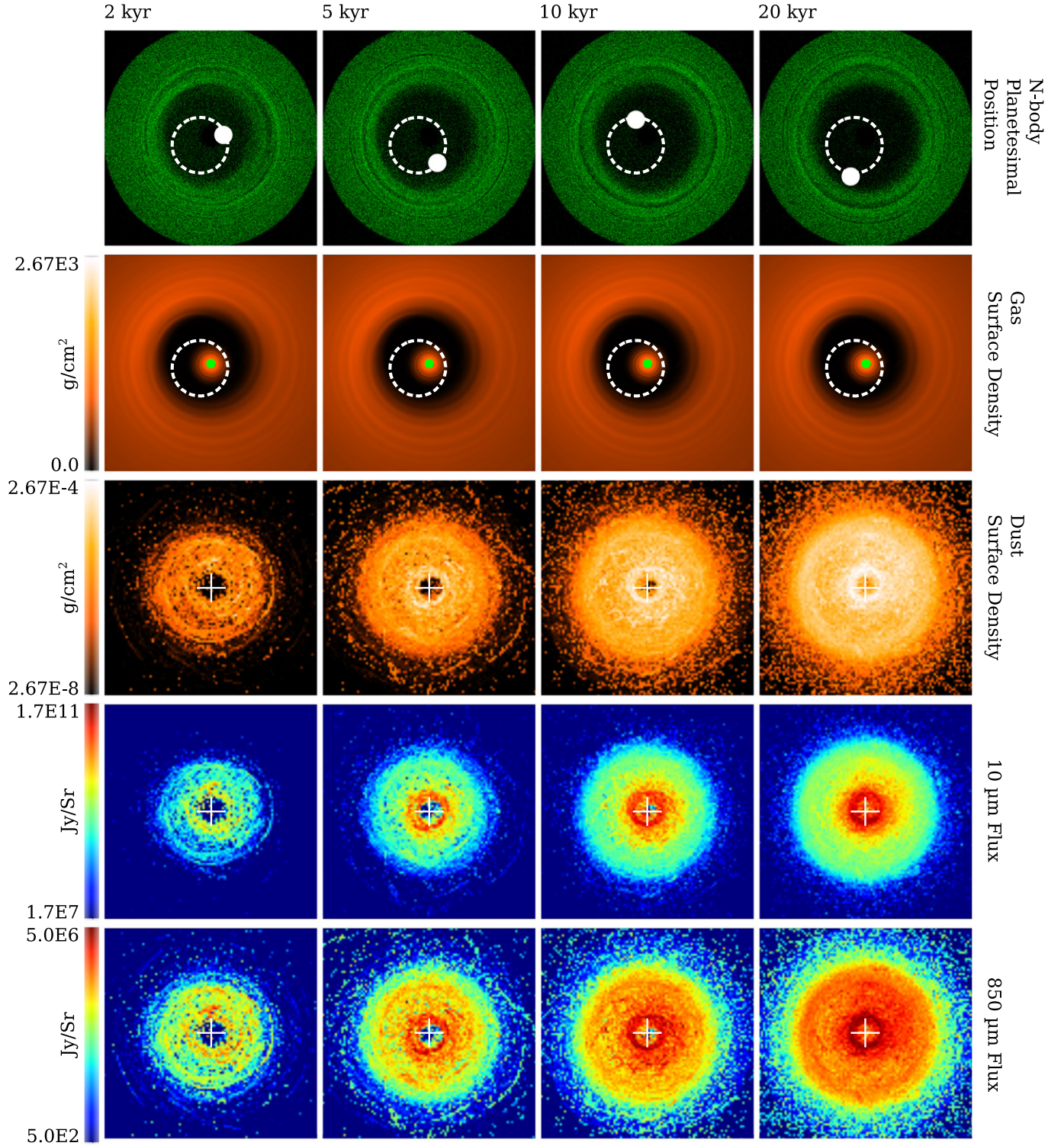


Figure 3. Summary of output from simulation 11. From top to bottom: positions of planetesimals over time, gas surface density from supporting FARGO simulations (green areas are outside the grid), dust surface density when lifetime is modeled as an exponential decay (decay constant of 10^4 yr), flux from dust (no stellar flux included) from radiative transfer modeling using RADMC3D at $10\ \mu\text{m}$ and at $850\ \mu\text{m}$. The white dotted line indicates the approximate orbit of the planet, the white circle indicates its approximate position, and the white cross indicates the barycenter of the system.

($F_{\text{disk}}/F_* \sim 1/100$). This is easily detectable by nulling interferometry, which can claim detections of exozodis with $F_{\text{disk}}/F_* \geq 10^{-4}$ in the *N*-band (Millan-Gabet et al. 2011), and could therefore also detect the no-planet cases. The survey conducted in Absil et al. (2013) was sensitive to $F_{\text{disk}}/F_* \geq 10^{-2}$ in the *K*-band, which would render our model

systems undetectable. However, our simulated disk was truncated at 0.8 AU for numerical reasons; if this restriction were relaxed the planetary cases might be marginally detectable. If a sufficient planetesimal population survives to late times, gravitational stirring is a possible source of young exozodis.

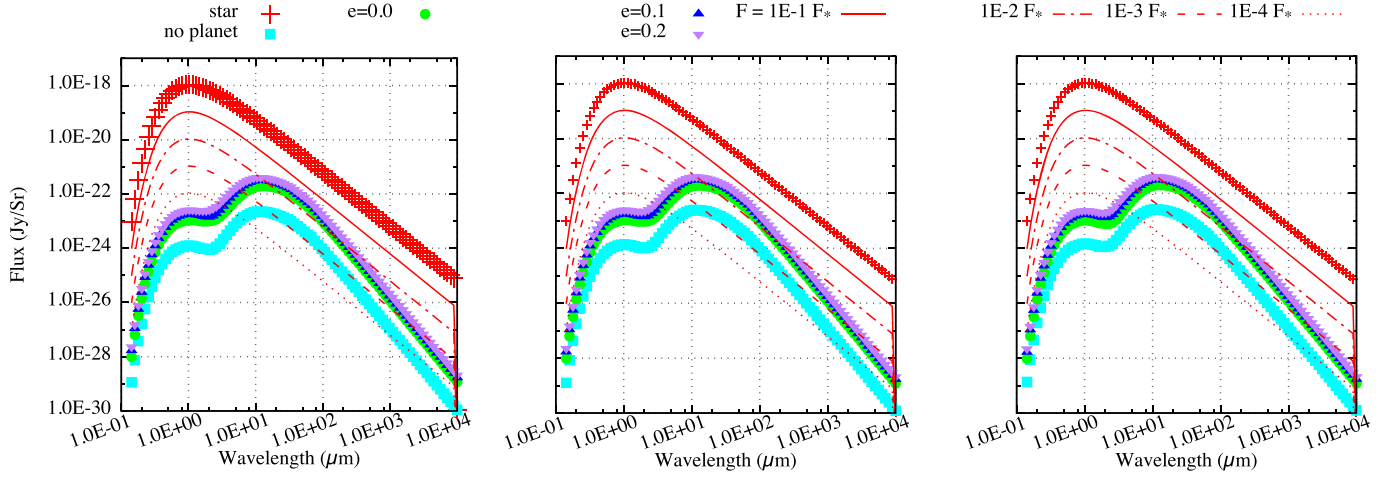


Figure 4. Spectrum of dust surface density with exponential decay applied (10^4 yr timescale). From left to right: no gas component, gas with small (1×10^{-5} m) fragments, gas with large (1×10^{-3} m) fragments. Red “+” signs are the stellar flux, other markers are different simulations. Lines (solid, dotted–dashed, dashed, dotted) are guide lines showing different fractions of stellar flux. All frames are taken at 20 kyr, with a 10 kyr decay constant, and computed with RADMC3D.

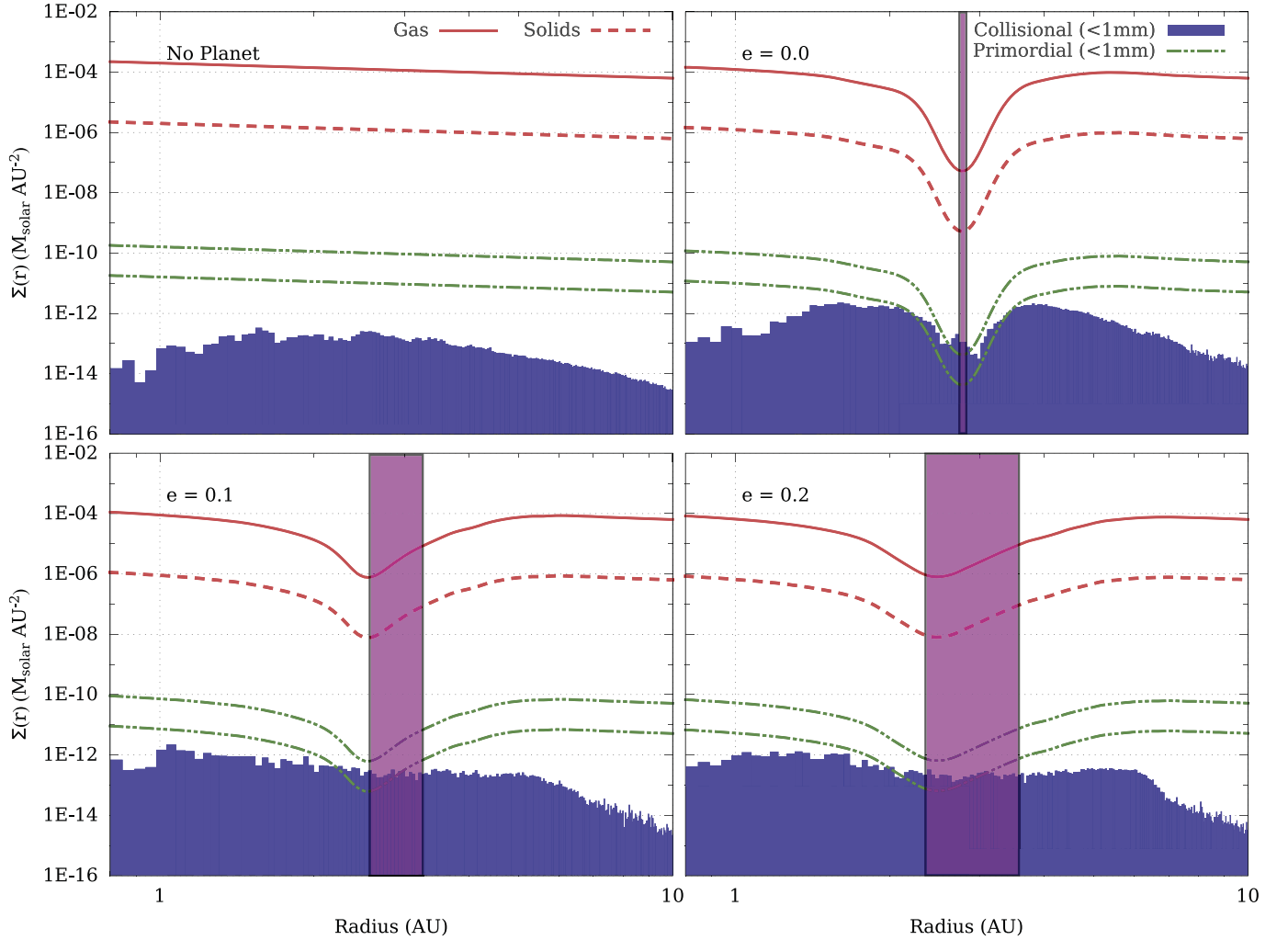


Figure 5. Dust surface density against radius for each of the four main simulations. The solid red line is the gas surface density, the dotted red line is the solid material assuming a 100:1 gas to solids ratio, the green dotted–dashed line (with fill pattern) is an estimate for the surface density of small (<1 mm) dust, and blue bars are the collisional material from the indicated simulations. All frames are taken at the end of the simulations. The orbital extent of the planet is depicted with the magenta rectangle, with inner and outer edges corresponding to periastron and apastron, respectively.

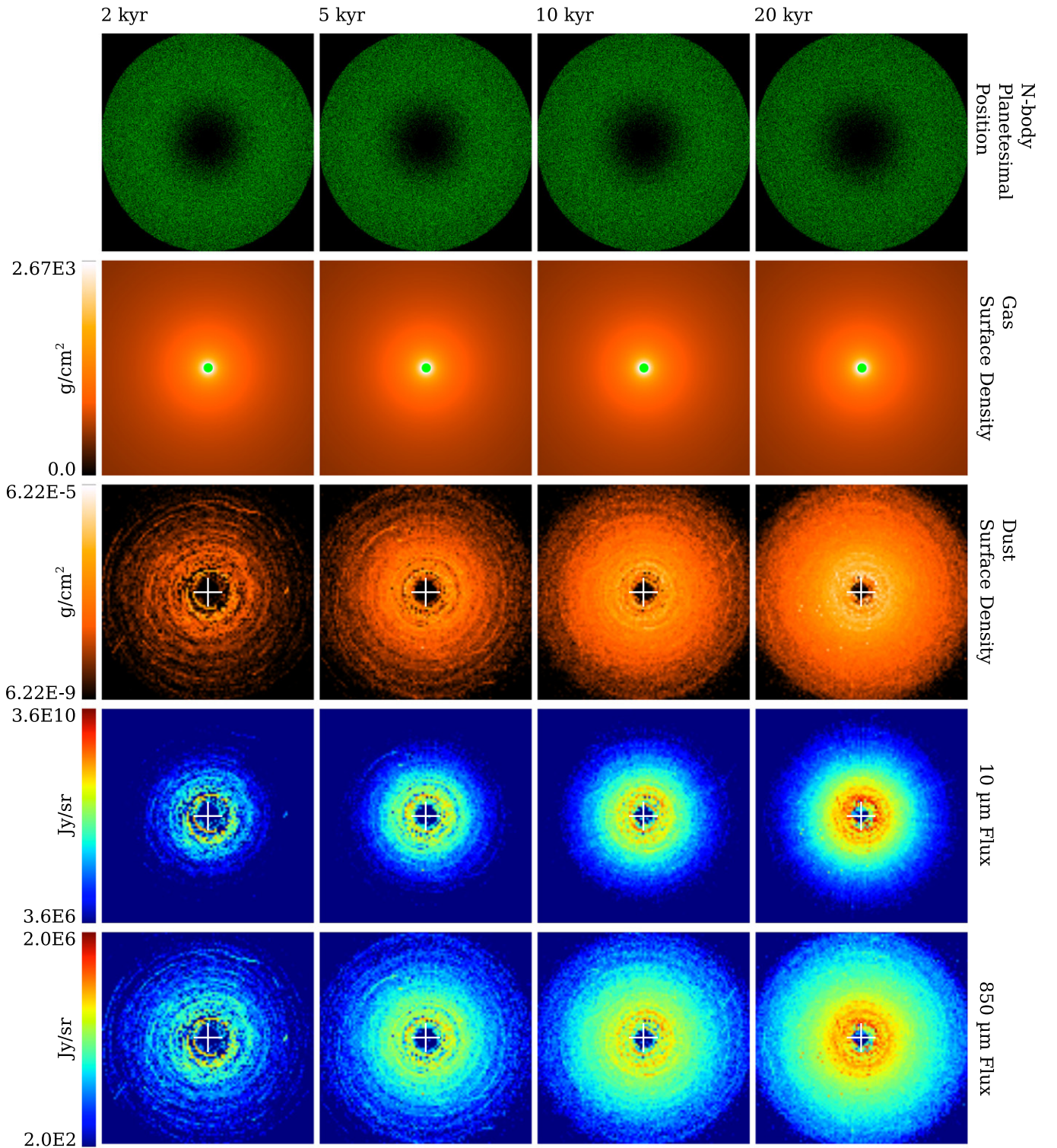


Figure 6. Summary of output from simulation 2. From top to bottom: Positions of planetesimals over time, gas surface density from supporting FARGO simulations (green areas are outside the grid), dust surface density when lifetime is modeled as an exponential decay (decay constant of 10^4 yr), flux from dust (no stellar flux included) from radiative transfer modeling using RADMC3D at $10\ \mu\text{m}$, flux from dust (no stellar flux included) from radiative transfer modeling using RADMC3D at $850\ \mu\text{m}$. The white cross indicates the barycenter of the system.

As this simulation spanned only 20,000 yr the long-term observability of these systems is unknown. Because of gravitational stirring, even a reduction in collision rate may keep the planetary cases observable due to the higher proportion of violently erosive collisions, which are the main

generator of dust, and an overall decrease in primordial dust mass over time.

The planetesimals simulated are of the order ~ 100 km, and we have assumed that these are not affected significantly by aerodynamic drag. This is justified on the timescales of our

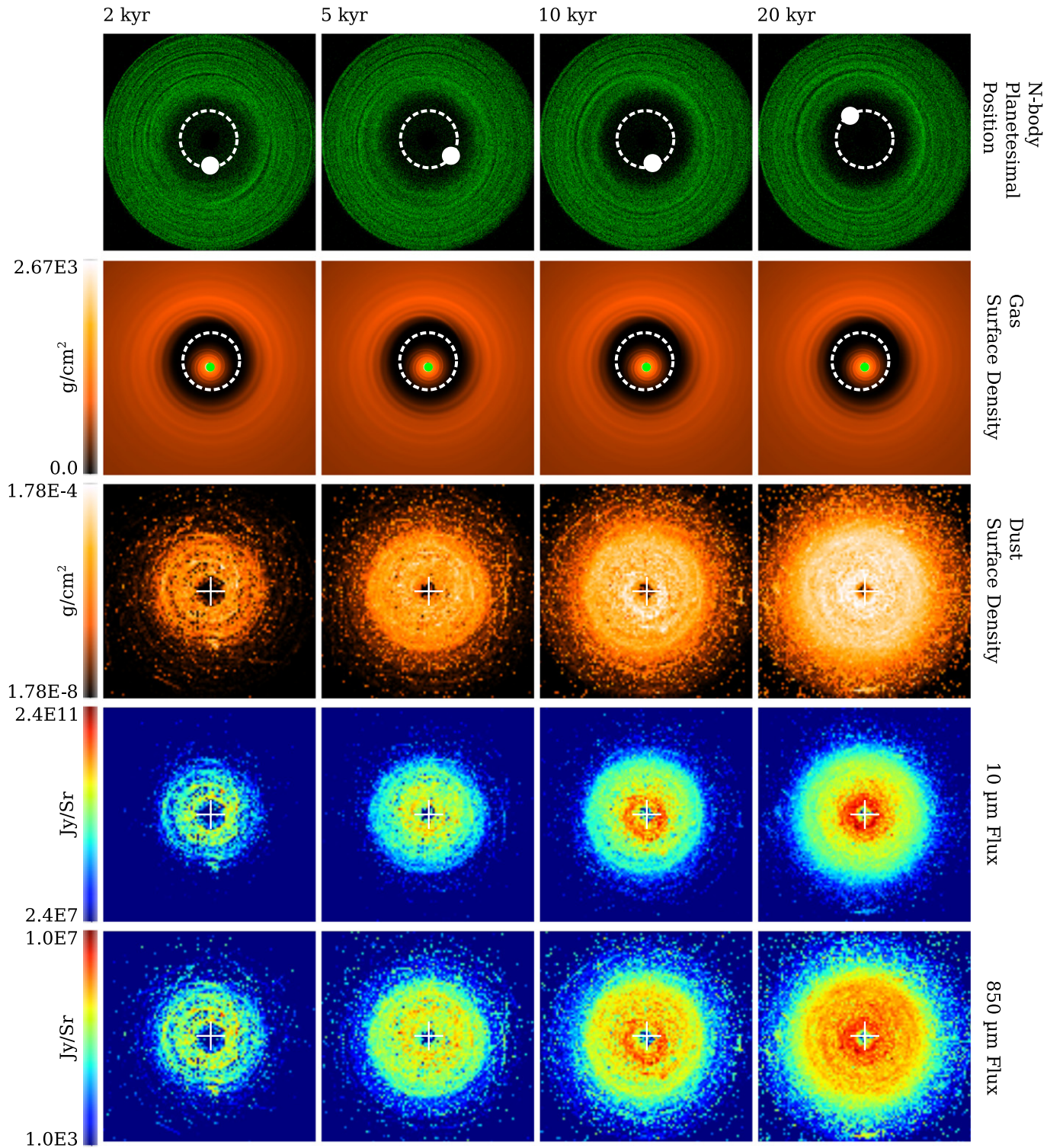


Figure 7. Summary of output from simulation 8. From top to bottom: positions of planetesimals over time, gas surface density from supporting FARGO simulations (green areas are outside the grid), dust surface density when lifetime is modeled as an exponential decay (decay constant of 10^4 yr), flux from dust (no stellar flux included) from radiative transfer modeling using RADMC3D at $10\ \mu\text{m}$, flux from dust (no stellar flux included) from radiative transfer modeling using RADMC3D at $850\ \mu\text{m}$. The white dotted line indicates the approximate orbit of the planet, the white circle indicates its approximate position, and the white cross indicates the barycenter of the system.

simulations, but eccentric planetesimals can become circularized on ~ 1 Myr timescales and migrate on ~ 5 Myr timescales (Grishin & Perets 2015). Far from the perturbing planet, this will cause a decrease in the planetesimal collision rate; however, when the perturbations from the planet are

strong (which is the case in this work) the authors argue that the planetesimals will retain their eccentric orbits. The long-term behavior of eccentric planetesimals in the vicinity of a planet and under the influence of aerodynamic drag should be investigated in future work because the long-

term observability of a system is tied to the collision frequency.

Interestingly, the presence of gas in the simulations does not change the SED substantially (Figure 4). This may be caused by fragments being stirred by the planet on a much shorter timescale than the gas entrainment timescale. Or possibly the gas near the planet is perturbed in the same manner as the fragments, such that entrainment does happen but is qualitatively identical to the no-gas case. However, the presence of gas does “wash out” any non-axisymmetric structures in the eccentric simulations.

In the earlier phases of the simulation bright spots and arcs of dust are easily visible in the plots of dust surface density. As time moves on, these structures, while still present, are more difficult to observe. In all cases, they are due to collisions that occurred just prior to the frame in question and the fragments have not had sufficient time to spread over their orbit. Possibly this is analogous to bright spots seen in debris disks recorded by Su et al. (2015).

The double ring structure of a zero-eccentricity planet would be detectable with ALMA if gas were depleted by an order of magnitude with respect to a protoplanetary disk, thus providing a sensitivity of $10 \mu\text{Jy}$ with a five-hour observation under ideal circumstances (Yatagai 2011).

5. CONCLUSION

In this work we present results from four simulations (Table 1), each of which has had its second-generation dust modeled in three separate ways (Table 2). All simulations were integrated with the PKDGRAV code using the EDACM collision model. During these simulations each collision was recorded, and a modified version of the EDACM collision model was used to produce small dust fragments with accurate velocities. The orbits of the dust fragments were integrated with a simple N -body code using the kick-drift version of the leapfrog integrator and split across multiple processors. The resulting dust density was post-processed to account for a 10^4 yr dust lifetime (measured from the moment of the generating collision) and passed to RADMC3D for radiative transfer modeling.

The presence of gas was simulated by running an analogous FARGO simulation for each PKDGRAV simulation. Once a quasi-steady state was reached, the gas density and velocity fields were included in the fragment simulations. The presence of gas had no significant effect upon second-generation dust distribution over the time simulated. However, a reduction, or “wash out,” of non-axisymmetric structures is observed when gas is included.

Dust production is enhanced by the presence of a planetary body by a factor of ~ 10 (Figure 4). Also, the main source of second-generation dust comes from erosive collisions rather than the more common partially accretive collisions. The collisional material has a similar fractional luminosity as exozodis. If a planetesimal population is present in a system at a late time, second-generation dust would be detectable with nulling interferometry (Millan-Gabet et al. 2011; Absil et al. 2013).

Second-generation dust as a marker for the presence of an unobserved planetary companion would be visible with ALMA. In the case of a circular planet in a system with gas depleted by an order of magnitude with respect to a

protoplanetary disk, observations with ALMA would be able to detect a double ring structure (Figure 2).

J.D. is grateful for support from NERC, Bristol School of Physics, and McDonald Observatory. Z.M.L. is supported by a STFC Advanced Fellowship. S.D.R. is supported by National Science Foundation CAREER award AST-1055910. N.A.T. is supported by the UK Space Agency/STFC. This work was carried out using the computational facilities of the Advanced Computing Research Centre, University of Bristol. Also, thanks goes to the anonymous referee, whose suggestions have been immensely helpful.

REFERENCES

- Absil, O., Defrère, D., Coudé du Foresto, V., et al. 2013, *A&A*, **555**, A104
 Adams, F. C., Hollenbach, D., Laughlin, G., & Gorti, U. 2004, *ApJ*, **611**, 360
 Bai, X.-N., & Stone, J. M. 2010, *ApJ*, **722**, 1437
 Bromley, B. C., & Kenyon, S. J. 2011, *ApJ*, **731**, 101
 Burns, J. A., Lamy, P. L., & Soter, S. 1979, *Icar*, **40**, 1
 Chambers, J. E., & Wetherill, G. W. 1998, *Icar*, **136**, 304
 Crida, A., Morbidelli, A., & Masset, F. 2006, *Icar*, **181**, 587
 Cuzzi, J. N., Hogan, R. C., & Shariff, K. 2008, *ApJ*, **687**, 1432
 D’Alessio, P., Cantö, J., Calvet, N., & Lizano, S. 1998, *ApJ*, **500**, 411
 Dobinson, J., Leinhardt, Z. M., Dodson-Robinson, S. E., & Teanby, N. A. 2013, *ApJL*, **777**, L31
 Dodson-Robinson, S. E., & Salyk, C. 2011, *ApJ*, **738**, 131
 Dong, R., Zhu, Z., & Whitney, B. 2015, *ApJ*, **809**, 93
 Dullemond, C. P., & Dominik, C. 2005, *A&A*, **434**, 971
 Espaillat, C., Muzerolle, J., Najita, J., et al. 2014, in *Protostars and Planets VI*, ed. H. Beuther et al. (Tucson, AZ: Univ. of Arizona Press), 497
 Fouchet, L., Gonzalez, J.-F., & Maddison, S. T. 2010, *A&A*, **518**, A16
 Fouchet, L., Maddison, S. T., Gonzalez, J.-F., & Murray, J. R. 2007, *A&A*, **474**, 1037
 Goldreich, P., & Tremaine, S. 1980, *ApJ*, **241**, 425
 Gonzalez, J.-F., Pinte, C., Maddison, S. T., Ménard, F., & Fouchet, L. 2012, *A&A*, **547**, A58
 Gressel, O., Nelson, R. P., & Turner, N. J. 2011, *MNRAS*, **415**, 3291
 Grishin, E., & Perets, H. B. 2015, arXiv:1511.07435
 Hartmann, L., Calvet, N., Gullbring, E., & D’Alessio, P. 1998, *ApJ*, **495**, 385
 Hayashi, C. 1981, *PTPS*, **70**, 35
 Hayashi, C., Nakazawa, K., & Nakagawa, Y. 1985, in *Protostars and Planets II*, ed. D. C. Black, & M. S. Matthews (Tucson, AZ: Univ. of Arizona Press), 1100
 Hernán-Obispo, M., Gálvez-Ortiz, M. C., Anglada-Escudé, G., et al. 2010, *A&A*, **512**, A45
 Johansen, A., Klahr, H., & Henning, T. 2006, *ApJ*, **636**, 1121
 Johansen, A., & Lacerda, P. 2010, *MNRAS*, **404**, 475
 Jones, M. G., Pringle, J. E., & Alexander, R. D. 2012, *MNRAS*, **419**, 925
 Kokubo, E., & Ida, S. 2000, *Icar*, **143**, 15
 Kral, Q., Thébaud, P., & Charnoz, S. 2013, *A&A*, **558**, A121
 Kruegel, E. 2003, *The Physics of Interstellar Dust* (Bristol: The Institute of Physics)
 Lambrechts, M., & Johansen, A. 2012, *A&A*, **544**, A32
 Leinhardt, Z. M., Dobinson, J., Carter, P. J., & Lines, S. 2015, *ApJ*, **806**, 23
 Leinhardt, Z. M., & Richardson, D. C. 2005, *ApJ*, **625**, 427
 Leinhardt, Z. M., Richardson, D. C., Lufkin, G., & Haseltine, J. 2009, *MNRAS*, **396**, 718
 Leinhardt, Z. M., & Stewart, S. T. 2012, *ApJ*, **745**, 79
 Levison, H. F., Duncan, M. J., & Thommes, E. 2012, *AJ*, **144**, 119
 Levison, H. F., Kretke, K. A., & Duncan, M. J. 2015, *Natur*, **524**, 322
 Masset, F. 2000, *A&AS*, **141**, 165
 Millan-Gabet, R., Serabyn, E., Mennesson, B., et al. 2011, *ApJ*, **734**, 67
 Morbidelli, A., Bottke, W. F., Nesvorný, D., & Levison, H. F. 2009, *Icar*, **204**, 558
 Morbidelli, A., Crida, A., Masset, F., & Nelson, R. P. 2008, *A&A*, **478**, 929
 Nelson, R. P., & Gressel, O. 2010, *MNRAS*, **409**, 639
 Nichols, E. F., & Hull, G. F. 1903, *ApJ*, **17**, 315
 Ormel, C. W., & Klahr, H. H. 2010, *A&A*, **520**, A43
 Owen, J. E. 2014, *ApJ*, **789**, 59
 Paardekooper, S.-J., & Leinhardt, Z. M. 2010, *MNRAS*, **403**, L64
 Paardekooper, S.-J., & Mellema, G. 2004, *A&A*, **425**, L9

- Paardekooper, S.-J., & Mellema, G. 2006, [A&A](#), **453**, 1129
- Pinilla, P., Benisty, M., Birnstiel, T., et al. 2014, [A&A](#), **564**, A51
- Pinilla, P., Birnstiel, T., Ricci, L., et al. 2012, [A&A](#), **538**, A114
- Pinilla, P., de Juan Ovelar, M., Ataiee, S., et al. 2015, [A&A](#), **573**, A9
- Raymond, S. N., O'Brien, D. P., Morbidelli, A., & Kaib, N. A. 2009, [Icar](#), **203**, 644
- Rice, W. K. M., Armitage, P. J., Wood, K., & Lodato, G. 2006, [MNRAS](#), **373**, 1619
- Richardson, D. C., Quinn, T., Stadel, J., & Lake, G. 2000, [Icar](#), **143**, 45
- Robertson, H. P. 1937, [MNRAS](#), **97**, 423
- Ruge, J. P., Wolf, S., Uribe, A. L., & Klahr, H. H. 2014, [A&A](#), **572**, L2
- Saar, S. H., & Donahue, R. A. 1997, [ApJ](#), **485**, 319
- Setiawan, J., Weise, P., Henning, T., et al. 2007, [ApJL](#), **660**, L145
- Spaute, D., Weidenschilling, S. J., Davis, D. R., & Marzari, F. 1991, [Icar](#), **92**, 147
- Stadel, J. G. 2001, PhD thesis, Univ. Washington
- Su, K. Y. L., Morrison, S., Malhotra, R., et al. 2015, [ApJ](#), **799**, 146
- Takami, M., Hasegawa, Y., Muto, T., et al. 2014, [ApJ](#), **795**, 71
- Thebault, P., Kral, Q., & Augereau, J.-C. 2014, [A&A](#), **561**, A16
- Weidenschilling, S. J. 1977, [MNRAS](#), **180**, 57
- Weidenschilling, S. J., Spaute, D., Davis, D. R., Marzari, F., & Ohtsuki, K. 1997, [Icar](#), **128**, 429
- Wetherill, G. W., & Stewart, G. R. 1989, [Icar](#), **77**, 330
- Wyatt, M. C. 2008, [ARA&A](#), **46**, 339
- Yatagai, H. 2011, ALMA Sensitivity Calculator, Online Resource
- Zhu, Z., Nelson, R. P., Dong, R., Espaillat, C., & Hartmann, L. 2012, [ApJ](#), **755**, 6